

## Stationary and oscillatory convection of binary fluids in a porous medium

M. Augustin, R. Umla, B. Huke, and M. Lücke

*Institut für Theoretische Physik, Universität des Saarlandes, Postfach 151150, D-66041 Saarbrücken, Germany*

(Received 2 July 2010; published 4 November 2010)

We investigate numerically stationary convection and traveling wave structures of binary fluid mixtures with negative separation ratio in the Rayleigh-Bénard system filled with a porous medium. The bifurcation behavior of these roll structures is elucidated as well as the properties of the velocity, temperature, and concentration fields. Moreover, we discuss lateral averaged currents of temperature and concentration. Finally, we investigate the influence of the Lewis number, of the separation ratio, and of the normalized porosity on the bifurcation branches.

DOI: [10.1103/PhysRevE.82.056303](https://doi.org/10.1103/PhysRevE.82.056303)

PACS number(s): 47.56.+r, 47.20.Bp, 47.54.-r

### I. INTRODUCTION

Binary fluid mixtures such as ethanol-water,  $^3\text{He}$ - $^4\text{He}$ , or various gas mixtures show already at small heating rates a rich variety of convection patterns when heated from below, which cannot be observed in pure fluids. In such mixtures, the concentration field enters the dynamics via the so-called Soret effect, i.e., the driving of concentration currents due to temperature gradients. A popular setup to investigate pattern formation and bifurcation scenarios in binary mixtures is the Rayleigh-Bénard system. The system consists of a fluid layer bounded by two horizontal plates which are held at constant but different temperatures. A great deal of experimental as well as theoretical research has been focused on this system and many different convection patterns have been found. For a review see, e.g., [1–3].

In this paper, we investigate a modification of the Rayleigh-Bénard system: the gap between the plates is filled here by a porous medium which is saturated by a fluid. For a pure fluid, first investigations of this system have been performed by Horton and Rogers [4] as well as by Lapwood [5] who investigated the stability of the ground state. Later on, Straus [6] and Juárez and Busse [7] theoretically investigated so-called Bénard rolls or steady overturning convection (SOC) structures and their stability. Roll convection was also observed in experiments with a pure fluid in a system filled with a porous medium by Shattuck *et al.* [8] and Howle *et al.* [9].

Further research concerning binary mixtures in porous media has been done by Charrier-Mojtabi *et al.* [10], Elhajjar *et al.* [11], and Sovran *et al.* [12]. They investigated the ground state and found two kinds of stability thresholds: a stationary one and an oscillatory one. The latter arises only for negative Soret coupling, i.e., when the heavier component tends toward regions of higher temperature, e.g., toward the lower plate.

The understanding of the spatiotemporal behavior of binary fluid convection in porous media is of relevance for industrial applications, e.g., for the modeling of oil and gas reservoirs [13–15] or for transport processes in geothermal reservoirs [16]. Unsatisfactory modeling with a lack of knowledge of the basics of convective structure formation can lead to suboptimal efficiency for the description or premature exploitation of reservoirs. Furthermore, flow in po-

rous media is of interest in chemical and engineering industries, e.g., in absorption and adsorption processes, heat storage, nuclear reactors, and spacecraft thermal management systems [17]. Moreover, convection in porous media is also of interest from the viewpoint of basic science: filling the standard Rayleigh-Bénard system with a porous medium can give rise to new instability mechanisms and possibly new convection structures [18].

Here, we investigate binary mixtures with negative Soret coupling. For such fluids many convection patterns are known to be realized in the Rayleigh-Bénard setup without porous medium: there are spatially extended traveling waves (TW) and spatially localized traveling waves (LTW) [19–32], standing waves (SW) [33], and spatially localized SOC structures [34,35].

The knowledge about binary mixtures showing a negative Soret effect in the system with porous medium is less developed. Brand and Steinberg [36] investigated the stability of the ground state using a simple perturbation model. Knobloch [37] discussed bifurcation scenarios using amplitude equations. Numerical investigations on the stability of the ground state have been performed by Charrier-Mojtabi *et al.* [10], Elhajjar *et al.* [11], and Sovran *et al.* [12] as mentioned above.

As a guide to the investigation of convection structures in systems with a porous medium that is filled with a binary mixture with negative Soret effect we found it useful to look first for convection patterns that are known from the common Rayleigh-Bénard system without porous medium. In order to do so, we carried out numerical studies focusing on two simple spatially periodic structures: stationary overturning convection (SOC) and traveling waves (TW), both in the form of straight rolls without spatial variation along the direction of the roll axes. These flows are two-dimensional and the pattern associated with the convection structure is one-dimensional. Its wave vector is oriented perpendicular to the roll axes and it is constant in space and time. Roll convection in binary fluids with positive Soret coupling in the presence of a porous medium has been studied recently by the authors of this paper [18].

The paper is organized as follows: in Sec. II we discuss the system, the fields, the governing equations and the numerical methods. Moreover, we discuss the impossibility of a mean flow. We give a short review of the ground state, and we introduce some order parameters. In Sec. III, we discuss

the bifurcation behavior of TW and SOC solutions and the field properties of velocity, temperature, and concentration in TWs and the lateral currents in a TW for an exemplary set of parameters. The influence of the Lewis number  $L$ , separation ratio  $\psi$ , and normalized porosity  $\phi^*$  on the bifurcation behavior is the subject of Sec. IV. We conclude in Sec. V.

## II. FOUNDATIONS

### A. System and basic equations

Here we give only a brief summary of the system and the governing equations. For more details see [18]. We consider two infinite parallel plates perpendicular to a homogeneous gravitational field in  $z$  direction. Both plates are impermeable and perfectly heat conducting. The temperature at the plates is fixed. The space between the plates is filled with a porous medium which is considered to be isotropic and homogeneous. The porous medium is saturated with a binary fluid mixture. Moreover, we assume local thermal equilibrium between the fluid and the porous medium.

We used the following nondimensional balance equations

$$\nabla \cdot \mathbf{u} = 0, \quad (1a)$$

$$\gamma_a \partial_t \mathbf{u} = -\nabla p - \mathbf{u} + (\theta + c) \mathbf{e}_z, \quad (1b)$$

$$\partial_t \theta + \mathbf{u} \cdot \nabla \theta = R w + \nabla^2 \theta, \quad (1c)$$

$$\phi^* \partial_t c + \mathbf{u} \cdot \nabla c = R \psi w + L \nabla^2 (c - \psi \theta), \quad (1d)$$

assuming the Oberbeck-Boussinesq approximation to be valid. Here, convection is described by the Darcy velocity  $\mathbf{u} = (u, v, w)$ , the deviation  $\theta$  of the temperature field  $T$  from its linear ground state profile  $T_{\text{cond}}$ , the deviation  $c$  of the concentration field  $C$  from its linear ground state profile  $C_{\text{cond}}$ , and the pressure  $p$ . For roll convection with axes oriented in  $y$  direction all these fields do not depend on  $y$  and furthermore  $v=0$ . In the conductive ground state, the fields of velocity, temperature, and concentration are

$$\mathbf{u}_{\text{cond}} = 0, \quad T_{\text{cond}}(z) = T_0 - Rz, \quad C_{\text{cond}}(z) = C_0 + R\psi z, \quad (2)$$

respectively.

The parameters are the Lewis number  $L$  which is the quotient of solutal and thermal diffusion time, the Rayleigh-Darcy number  $R$  which measures the temperature difference between the plates, and the separation ratio  $\psi$  which measures the strength and direction of the Soret effect. The parameters  $\gamma_a$  and  $\phi^*$  are specific for the system with a porous medium.  $\gamma_a$  consists of the ratio of the time scale corresponding to the friction term  $-\mathbf{u}$  and the temperature diffusion time of the whole medium [38] multiplied by a correction factor which is needed for the sake of consistency between a description by the Darcy equation and experimental results [39].  $\gamma_a$  is usually very small and its exact value has therefore no relevant influence on the dynamics. It is fixed to 0.0001 for all calculations presented in this paper. Changes for even smaller  $\gamma_a$  turned out to be negligible. The

normalized porosity  $\phi^*$  is the product of the porosity and the ratio of the heat capacities of the fluid and the whole system. Multiplying the time derivative of concentration in Eq. (1d),  $\phi^*$  sets the time scales for changes in  $c$  relative to those in  $\theta$ .  $\phi^*$  falls between 0 and 1.

The assumption of impermeable and ideal heat conducting plates leads to the boundary conditions [18]

$$w = \theta = \partial_z (c - \psi \theta) = 0 \quad \text{at} \quad z = \pm \frac{1}{2}. \quad (3)$$

### B. Mean flow dynamics

In binary fluid mixtures without a porous medium, TW convection induces a lateral mean flow [40–42]. In this subsection we study whether a mean flow can also be generated without imposing a pressure gradient in the system with a porous medium. To that end we decompose the velocity field

$$\mathbf{u}(x, z, t) = \hat{\mathbf{u}}(x, z, t) + U(z, t) \mathbf{e}_x, \quad (4)$$

where  $U(z, t) \mathbf{e}_x = \langle \mathbf{u}(x, z, t) \rangle_x$  is the mean flow contribution and  $\hat{\mathbf{u}}(x, z, t) = \mathbf{u}(x, z, t) - U(z, t) \mathbf{e}_x$ , i.e.,  $\langle \hat{\mathbf{u}}(x, z, t) \rangle_x = 0$ . Here,  $\langle \dots \rangle_x$  denotes the lateral average in  $x$ -direction. By taking the lateral average of the  $x$ -component of Eq. (1b) and assuming that there is no pressure gradient imposed onto the system, we get

$$\gamma_a \partial_t U(z, t) = -U(z, t) \quad (5)$$

as equation of motion for the lateral mean flow. Consequently, any mean flow will be quickly damped exponentially. Unlike the nonlinear Navier-Stokes equation the linear momentum balance [Eq. (1b)] in the porous medium does not allow for nonlinear Reynolds stresses that could sustain a mean flow. Not being interested in transients, we thus take  $U=0$ .

### C. Numerical method

As mentioned before, the impermeability of the plates yields the boundary condition

$$\partial_z (c - \psi \theta) = 0, \quad (6)$$

which couples  $\theta$  and  $c$ . In order to get independent boundary conditions, one introduces the field

$$\zeta = c - \psi \theta. \quad (7)$$

The corresponding balance equation can directly be derived by combining Eqs. (1c) and (1d).

In addition, one can simplify the numerical treatment of Eq. (1b) by introducing two scalar potentials  $\Phi$  and  $\Psi$  such that  $\mathbf{u}$  can be written as

$$\mathbf{u} = \nabla \times \nabla \times (\Phi \mathbf{e}_z) + \nabla \times (\Psi \mathbf{e}_z), \quad (8)$$

which is possible because of the incompressibility condition [Eq. (1a)]. Equations for  $\Phi$  and  $\Psi$  can be derived by applying the curl to the momentum balance Eq. (1b) once or twice and taking the  $z$ -component in both cases. This yields

$$\gamma_a \partial_t \Delta_{xy} \Psi = -\Delta_{xy} \Psi, \quad (9a)$$

$$\gamma_a \partial_t \nabla^2 \Delta_{xy} \Phi = -\nabla^2 \Delta_{xy} \Phi - \Delta_{xy}(\theta + c), \quad (9b)$$

with  $\Delta_{xy} = \partial_x^2 + \partial_y^2$ . Note that these equations do not contain a pressure term anymore. As mentioned before, we do not investigate the behavior of fast transients. Therefore we can fix  $\Psi = 0$  and neglect Eq. (9a).

According to the boundary condition for  $\mathbf{u}$ , the boundary condition for  $\Phi$  is given by

$$\Phi = 0 \quad \text{at } z = \pm \frac{1}{2}. \quad (10)$$

### 1. Traveling waves

Here we discuss temporally and spatially periodic TW structures. To obtain such solutions, we used a Galerkin method with the ansatz

$$X(x, z) = \sum_m \sum_n (X_{mn} e^{im(kx - \omega t)} + \text{c.c.}) f_n(z) \quad (11)$$

for the fields  $X = \Phi, \theta, \zeta$ . Here  $k$  is the wave number and  $\omega$  the frequency of the TW state. The lateral index  $m$  starts from 0 for  $\theta$  and  $\zeta$  and from 1 for  $\Phi$ . To fix the phase of a TW structure we choose  $\Phi_{11} \in \mathbb{R}$ .

The functions  $f_n(z)$  appearing in Eq. (11) represent an orthonormal set of trigonometrical functions that fulfill the boundary conditions at the plates. We choose

$$\text{for } \Phi, \theta: f_n(z) = \begin{cases} \sqrt{2} \cos(n\pi z) & \text{if } n = 1, 3, 5, \dots \\ \sqrt{2} \sin(n\pi z) & \text{if } n = 2, 4, 6, \dots \end{cases} \quad (12)$$

$$\text{for } \zeta: f_n(z) = \begin{cases} \sqrt{2} \sin(n\pi z) & \text{if } n = 1, 3, 5, \dots \\ \sqrt{2} \cos(n\pi z) & \text{if } n = 2, 4, 6, \dots \\ 1, & \text{if } n = 0. \end{cases} \quad (13)$$

In Eq. (11), we can take advantage of some known symmetries of traveling waves [42]: (i) in a comoving frame of motion, TWs are stationary, i.e.,

$$X(x, z, t) = X(x - v_p t, z, 0) \quad (14)$$

with the phase velocity  $v_p = \frac{\omega}{k}$ . (ii) Right and left traveling wave solutions are symmetry degenerate. In this paper, we consider only right traveling waves. (iii) TWs are spatially periodic structures such that

$$X\left(x + \frac{2\pi}{k}, z, t\right) = X(x, z, t). \quad (15)$$

(iv) Furthermore, the TW structures also fulfill the so-called mirror glide symmetry [42]

$$X(x, z, t) = -X\left(x + \frac{\pi}{k}, -z, t\right). \quad (16)$$

This symmetry can be used to eliminate one half of the modes in Eq. (11).

These ‘‘macroscopic’’ symmetries of the TW solutions of the continuum balance equations can be expected to hold

despite the anisotropic and inhomogeneous character of the porous medium: we assume that the characteristic macroscopic length scale for convection, i.e., the layer height is much larger than the ‘‘microscopic’’ length scales that characterize the porous medium. Then inhomogeneities and anisotropies on the microscopic length scales can be expected not to disturb the macroscopic structure of TW convection.

For too large indices  $n, m$ , we truncate the expansion. According to our truncation scheme, all  $\theta$ - and  $\zeta$ -modes with  $n+m > N$  and all  $\Phi$ -modes with  $n+m > N/2$  are being neglected, where we choose  $N=32$  if not otherwise specified. The fact that the ansatz consists of less modes in  $\Phi$  than in  $\theta$  and  $\zeta$  is motivated by the work of Hollinger [44].

### 2. Stationary overturning convection

In this paper we also investigate, albeit more briefly, stationary roll solutions for negative separation ratios. SOC structures for positive separation ratios have been discussed by Umla *et al.* [18].

Stationary rolls fulfill like TW structures the spatial periodicity [Eq. (15)] and mirror glide symmetry [Eq. (16)]. Moreover, SOC structures are mirror symmetric in  $x$ -direction for an appropriate choice of  $x=0$  and they do not possess any time dependence. Therefore, to find roll solutions we use the ansatz

$$X(x, z) = \sum_m \sum_n X_{mn}^{\cos} \cos(mkx) f_n(z), \quad (17)$$

with  $f_n$  as defined above. The amplitudes  $X_{mn}$  of Eq. (11) and  $X_{mn}^{\cos}$  of Eq. (17) fulfill  $X_{mn}^{\cos} = 2 \operatorname{Re}(X_{mn})$ . For further details on the Galerkin method see [43].

### D. Ground state

The stability of the ground state has already been investigated by Sovran [12] and Mojtabi [10,11]. We reproduced their results by using a Galerkin expansion.

Figure 1 shows the critical Rayleigh-Darcy number  $R_c$ , the critical wave number  $k_c$ , and the Hopf frequency  $\omega_c$  of the oscillatory stability threshold as a function of  $\psi$  for different normalized porosities  $\phi^*$ . Here, we choose  $L=0.01$  which is a typical value for many liquids. For other values of  $L$ , the behavior of the oscillatory stability boundary was found to be similar.

As shown, the critical Rayleigh-Darcy number  $R_c$  increases with decreasing  $\phi$  as well as with decreasing  $\phi^*$ . The same holds true for the Hopf frequency  $\omega_c$  but not for the critical wave number— $k_c$  is only weakly dependent of  $\psi$  for  $\phi^*=1$  except for values of  $\psi$  near zero. As  $\phi^*$  decreases,  $k_c$  decreases for small values of  $|\psi|$  and increases for larger values of  $|\psi|$ . We do not include in Fig. 1 the stationary stability boundary which diverges for  $\psi \lesssim -0.01$  for the chosen  $L$  as can be shown analytically [11].

### E. Order parameters

We use the following order parameters to describe convective structures:

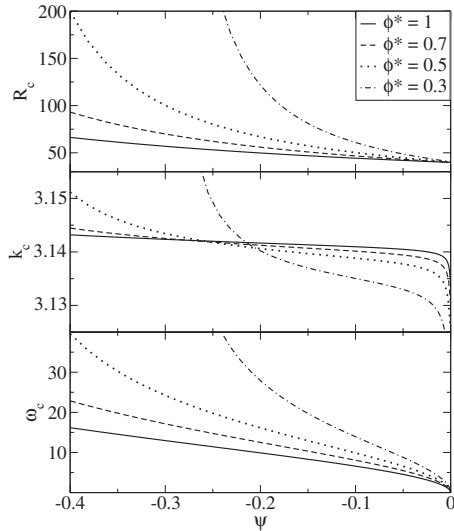


FIG. 1. Onset of oscillatory convection. From top to bottom the critical values of the Rayleigh-Darcy number,  $R_c$ , of the wave number,  $k_c$ , and of the Hopf frequency,  $\omega_c$ , are plotted versus  $\psi$  for different normalized porosities  $\phi^*$ . The Lewis number is in each case  $L=0.01$ .

(1) The leading amplitude  $w_{11}=k^2\Phi_{11}$  characterizes the vertical velocity field.

(2) The Nusselt number

$$\text{Nu} = \frac{\langle j_{T,z,\text{tot}} \rangle_x}{\langle j_{T,z,\text{cond}} \rangle_x} \quad (18)$$

measures the total vertical heat current density  $\langle j_{T,z,\text{tot}} \rangle_x$  relative to the conductive vertical heat current density  $\langle j_{T,z,\text{cond}} \rangle_x$ . Here,  $\langle \dots \rangle_x$  denotes the lateral average in  $x$ -direction. Note that the Nusselt number does not depend on  $z$  as long as we only consider SOC solutions and TW solutions which are stationary in the appropriate frame of reference. For structures which can be described by the ansatz [Eqs. (11) and (17)], respectively, the Nusselt number at the plates can be calculated from

$$\text{Nu} - 1 = -\frac{2\sqrt{2}\pi}{R} \sum_{n=1}^N (-1)^n n \theta_{0,2n}. \quad (19)$$

The behavior of  $\text{Nu}-1$  and  $w_{11}^2$  is qualitatively the same; we will mostly present and discuss plots for  $\text{Nu}$ .

(3) The mixing number

$$M = \frac{\sqrt{\langle C^2 \rangle - \langle C \rangle^2}}{\sqrt{\langle C_{\text{cond}}^2 \rangle - \langle C_{\text{cond}} \rangle^2}} \quad (20)$$

is the variance of the concentration field relative to its variance in the conductive state. Here,  $\langle \dots \rangle$  denotes the spatial average over the whole fluid layer. By definition, the value of  $M$  is equal to 1 in the ground state and  $M$  vanishes when the components of the binary fluid are perfectly mixed.

(4) TW states are furthermore characterized by their frequency  $\omega$ .

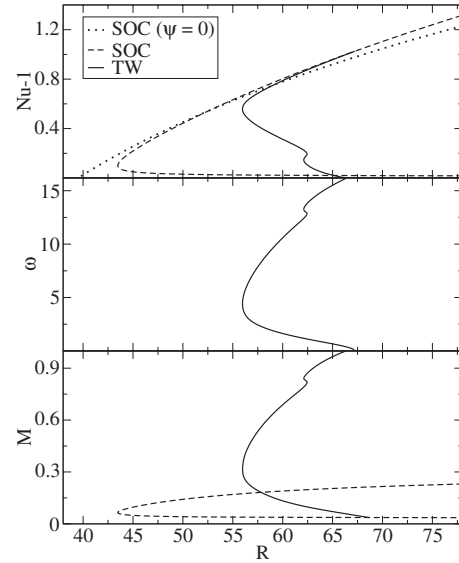


FIG. 2. Bifurcation behavior of TW- and SOC-solutions. From top to bottom we show  $\text{Nu}-1$  [Eq. (19)], the TW-frequency  $\omega$ , and the mixing number  $M$  [Eq. (20)] versus the Rayleigh-Darcy number  $R$ . Parameters are  $L=0.01$ ,  $\psi=-0.4$ , and  $\phi^*=1$ .

### III. GENERAL PROPERTIES OF TW AND SOC STATES

To discuss some basic properties of TW- and SOC-solutions we fix the parameters to  $L=0.01$ ,  $\psi=-0.4$ ,  $\phi^*=1$ , and  $k=\pi$  in this section. As mentioned before,  $L=0.01$  is a typical value for many liquids and  $\psi=-0.4$  can easily be realized using an ethanol-water mixture [45]. A wave number of  $k=\pi$  is close to the critical wave number, cf. Fig. 1.  $\phi^*=1$  corresponds to the case of a vanishing influence of the porous medium. In this case, the basic Eqs. (1) are almost the same as for a system without porous medium and infinite Prandtl number  $\sigma$  [43] except that the diffusion term  $\Delta \mathbf{u}$  in the velocity equation is replaced by a friction term  $-\mathbf{u}$ .

#### A. Bifurcation behavior

Figure 2 shows the Nusselt number  $\text{Nu}$  and the mixing number  $M$  of the TW- (solid line) and of the SOC-structure (dashed line) for the chosen parameters as well as the TW-frequency  $\omega$  as a function of  $R$ . For comparison, we also present the Nusselt number of a pure fluid (dotted line) which has already been investigated by Straus [6] and Juárez [7]. In the pure fluid case, TWs do not exist and SOCs bifurcate forward out of the ground state at the critical Rayleigh-Darcy number  $R_c^0=4\pi^2 \approx 39.48$  with the critical wave number  $k_c^0=\pi$ .

For binary mixtures with negative separation ratio, the situation is more complicated. The SOC solution branch is not connected anymore to the ground state as the stationary stability boundary of the ground state diverges already at much smaller values of  $|\psi|$ . Close to onset, i.e., for  $\text{Nu} \approx 1$ , the SOC branch runs backward until it reaches a saddle point. Afterward,  $\text{Nu}$  increases with increasing Rayleigh-Darcy number  $R$ . The mixing number  $M$  of the SOC structure is already relatively small on the backward branch and remains almost constant after the saddle point.

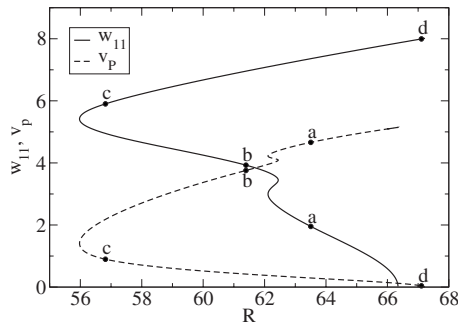


FIG. 3. The leading amplitude  $w_{11}$  of the vertical velocity field and the phase velocity  $v_p$  of TW solutions versus the Rayleigh-Darcy number  $R$ . The points labeled by a–d identify TW states for which fields and lateral profiles are shown in the corresponding subfigures of Fig. 4. Parameters are  $L=0.01$ ,  $\psi=-0.4$ , and  $\phi^*=1$ .

The TW branch bifurcates backward out of the ground state with a Hopf frequency of  $\omega_H \approx 16$ . For all parameter combinations discussed in this paper, the TW bifurcation is backward. This is in accordance with the results by Brand and Steinberg [36] who used an isosolutal boundary condition,  $c=0$ , at the plates, however. The TW branch soon reaches a first saddle point at  $R \approx 62.11$  and proceeds forward until it reaches a second saddle point at  $R \approx 62.44$ . The frequency of the TW structure along this short part of the solution branch is still rather large. Following the TW solution branch further on, we find a third saddle point at  $R \approx 56$ . Finally, the TW branch ends at the SOC branch at  $R^* \approx 67$  with zero frequency. The mixing number  $M$  of the TW structure as a function of  $R$  shows qualitatively the same behavior as the frequency  $\omega$  but ends at the SOC branch.

A very similar behavior of  $Nu$ ,  $M$  and  $\omega$  has already been described in the common Rayleigh–Bénard system without porous media, see e.g., [41,42]. In particular, Hollinger *et al.* [46] found a bistability of slow and fast traveling waves. Considering the similarities between the systems, we can suppose that, e.g., for values of the Rayleigh-Darcy number about 62, three of the six structures we found are stable: The conductive ground state, a fast TW structure with a phase velocity  $v_p$  of approximately 4.1, and a slow TW structure with  $v_p \approx 0.36$ .

### B. Structure of the fields

In this section we study the fields of temperature, concentration, and velocity of a TW along its bifurcation branch. Figure 3 shows the leading amplitude  $w_{11}$  of the vertical velocity as well as the phase velocity  $v_p = \omega/k$ . The Nusselt number shows qualitatively the same behavior as  $w_{11}^2$ .

States marked by dots labeled a–d in Fig. 3 are studied in more detail in the corresponding subfigures (a)–(d) of Fig. 4. Therein we show  $T$  and  $C$  as well as streamlines observed from a reference frame that is comoving with the TW. Additionally, Fig. 4 shows the lateral profiles of  $T$ ,  $C$ , and  $w$  at midheight, i.e., at  $z=0$ .

First, we discuss the lateral profiles. In Fig. 4(a), for the smallest amplitude, there is a phase difference between vertical velocity, temperature, and concentration. This phase dif-

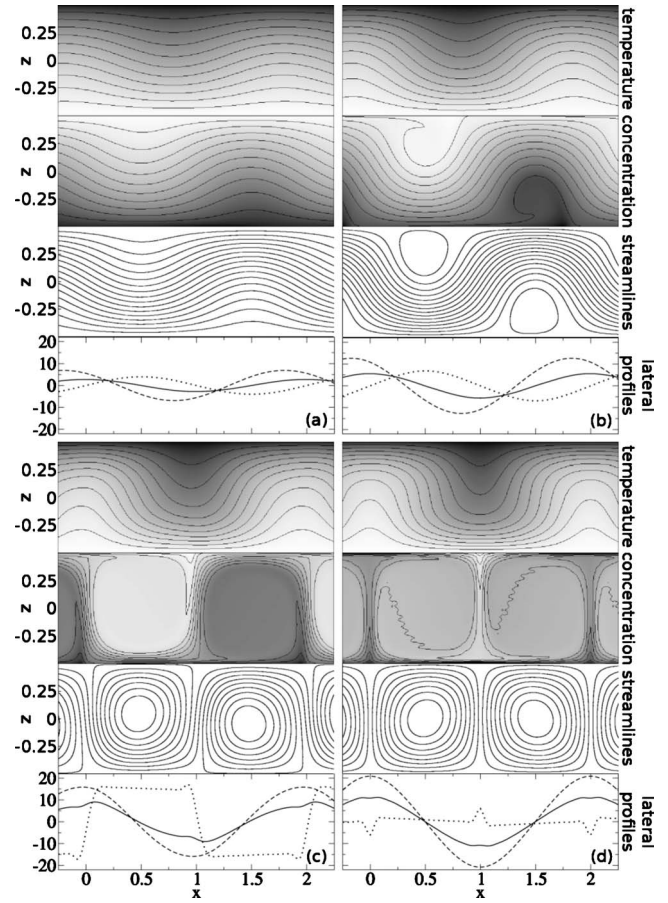


FIG. 4. Spatial structure of the TW solutions. The subfigures (a)–(d) correspond to the TW states that are identified by the points a–d in Fig. 3. In each subfigure we show from top to bottom the temperature distribution, the concentration distribution, the streamlines in a comoving frame, and the lateral profiles of  $w$  (full line),  $T$  (dashed line), and  $C$  (dotted line) at midheight,  $z=0$ . In (c) and (d) the concentration in the lateral profiles is multiplied for better visibility by a factor of 10. Light (dark) regions correspond to regions with high (low) temperature. Same holds true for the concentration distribution. Parameters are  $L=0.01$ ,  $\psi=-0.4$ , and  $\phi^*=1$ .

ference shrinks with growing amplitude [Figs. 4(b)–4(d)] and finally vanishes as the TW solution merges into the SOC state at  $R^*$ . The lateral temperature profile is nearly harmonic for all four states whereas the lateral profile of the vertical velocity component shows some anharmonicity at the maxima and minima in Figs. 4(c) and 4(d). The lateral profile of the concentration field shows the greatest changes. While it is harmonic in the states a and b, it becomes trapezoidal in c. In state d it is mainly constant apart from peaks where the fluid flows downward and dips where it flows upward. Note that the concentration profile Figs. 4(c) and 4(d) is multiplied by a factor 10 for better visibility.

The first row of Figs. 4(a)–4(d) shows the temperature distribution. Starting from the linear ground state profile, it becomes more and more modulated. Although the thermal driving in Fig. 4(d) is quite strong at  $R=67$ , the temperature field can still be well described by taking into account only a few modes.

The concentration field is shown in the second row of each subfigure in Fig. 4. The concentration isolines look similar to the streamlines of the TW structure in a comoving frame as shown in the third row of Figs. 4(a)–4(d). This similarity can be explained by the smallness of the Lewis number  $L$  [47,42]: the nondimensional equation for the concentration field  $\tilde{C}$  reads

$$(\tilde{\mathbf{u}} \cdot \tilde{\nabla})\tilde{C} = L\tilde{\nabla}^2(\tilde{C} - \psi\tilde{T}). \quad (21)$$

Since the Lewis number  $L$  is small, the diffusive term on the right hand side of Eq. (21) can be neglected. Thus, gradients of  $\tilde{C}$  have to be perpendicular to the direction of  $\tilde{\mathbf{u}}$ , i.e., the isolines of  $\tilde{C}$  are approximately identical to the streamlines of  $\tilde{\mathbf{u}}$ . Therefore, in order to explain the development of the concentration distribution along the TW bifurcation branch, we investigate the behavior of the streamlines. To simplify matters, we use a single-mode representation of the velocity field for the explanation. According to our ansatz [Eq. (11)] and for  $k=\pi$ , the velocity field  $\tilde{\mathbf{u}}$  in a comoving frame is given by

$$\tilde{u} = w_{11} \sin(\pi x) \sin(\pi z) - v_p, \quad (22)$$

$$\tilde{v} = 0, \quad (23)$$

$$\tilde{w} = w_{11} \cos(\pi x) \cos(\pi z). \quad (24)$$

With this we can define a stream function  $\tilde{\Psi}$  as

$$\tilde{\Psi} = -v_p z - \frac{w_{11}}{\pi} \sin(\pi x) \cos(\pi z). \quad (25)$$

Closed streamlines arise when local extrema of  $\tilde{\Psi}$  appear, which is equivalent to  $|v_p/w_{11}| < 1$ . Moreover, the positions of the centers of closed streamlines can be determined to be  $x=(4n+1)/2$ ,  $z=\arcsin(v_p/w_{11})$  and  $x=(4n+3)/2$ ,  $z=\arcsin(-v_p/w_{11})$ ,  $n \in \mathbb{Z}$ ,  $z \in [-0.5, 0.5]$ . Together with Fig. 3, this already explains the form of the streamlines in Fig. 4 very well. In state a we have  $v_p > w_{11}$ , so there are no closed streamlines. The TW b is located close to the intersection point of  $v_p$  and  $w_{11}$ . Here,  $w_{11}$  is only slightly larger than  $v_p$ . Therefore, the closed streamlines cover only small regions near the plates and do not intersect the line  $z=0$  while open streamlines meander around and between them. The roll-like regions of closed streamlines grow with decreasing phase velocity  $v_c$  [Figs. 4(c) and 4(d)]. Vice versa, the regions of open streamlines diminish until the only open streamlines remaining are the separatrices between the rolls of the final SOC state.

To explain the behavior of the concentration field, we take into account that there is approximately no exchange of concentration between regions of closed and regions of open streamlines. In the ground state, the Soret effect causes a concentration surplus at the upper plate (light gray in Fig. 4) and a lack of concentration at the lower plate (dark gray in Fig. 4). Thus, the rolls at the upper plate are fed only by fluid with high concentration and the rolls at the lower plate only by fluid with low concentration. Consequently, we observe in Fig. 4(b) two regions of almost homogeneous concentration

at two different levels. While the phase velocity  $v_p$  decreases, the regions of closed streamlines grow toward the opposite plate and the area of open streamlines shrinks. The concentration difference between adjacent rolls diminishes [Fig. 4(c)]. Finally, the fluid becomes homogeneously mixed everywhere except in the narrow boundary layers at the plates and between the rolls [Fig. 4(d)]. The peaks and dips in the lateral profile of the concentration in Fig. 4(d) originate from these boundary layers.

The above explanation is based on the smallness of the Lewis number  $L$  and the assumption that the concentration can thus be considered as a passively transported scalar. In particular, it is not valid if the diffusive term in Eq. (21) cannot be approximately neglected. In liquids  $L \ll 1$  is typically fulfilled.

### C. Lateral currents

Unlike SOC structures, TW states lack the left-right mirror symmetry between oppositely turning rolls. This allows the existence of lateral heat or concentration currents even though there is no mean flow in the system, see Sec. II B.

The lateral average of the lateral heat current density  $\langle j_{T,x} \rangle_x$  is given by

$$\langle j_{T,x} \rangle_x = \langle uT + \partial_x T \rangle_x. \quad (26)$$

Expressed in terms of  $\Phi$  and  $\theta$  one has

$$u = \partial_{zx} \Phi(x, z), \quad (27)$$

$$T = T_0 - Rz + \theta(x, z). \quad (28)$$

Inserting the representation Eq. (11) into Eq. (26) yields

$$\begin{aligned} \langle j_{T,x} \rangle_x &= \sum_{m=1}^{M_\Phi} \sum_{n=1}^{N_\theta} \sum_{l=1}^{N_\Phi} 4mk [\text{Im}(\theta_{mn}) \text{Re}(\Phi_{ml}) \\ &\quad - \text{Re}(\theta_{mn}) \text{Im}(\Phi_{ml})] f_n(z) \partial_z f_l(z). \end{aligned} \quad (29)$$

Here,  $\text{Re}$  denotes the real part and  $\text{Im}$  the imaginary part of a quantity with  $f_n$  and  $f_l$  as defined in Eq. (12). Obviously  $\langle j_{T,x} \rangle_x$  does vanish if all lateral modes are in phase. The same holds true for the lateral concentration current  $\langle j_{C,x} \rangle_x$ ,  $\Phi$  and  $c$ .

Figure 5 shows the laterally averaged lateral currents of heat,  $\langle j_{T,x} \rangle_x$ , and of concentration,  $\langle j_{C,x} \rangle_x$ , respectively, for the TW states a–d of Fig. 3. Both currents fulfill the symmetry

$$\langle j_x \rangle_x(-z) = -\langle j_x \rangle_x(z), \quad (30)$$

which follows from Eq. (29) and from the mirror glide symmetry [Eq. (16)]. Consequently, the total averages  $\langle j_{T,x} \rangle_{x,z}$  and  $\langle j_{C,x} \rangle_{x,z}$  vanish. In the upper half of the system, the heat current is parallel to the direction of propagation of the TW whereas the concentration current is antiparallel. These relations are reversed in the lower half.

The heat current  $\langle j_{T,x} \rangle_x$  always vanishes at  $z = \pm 0.5$  as a consequence of the boundary condition  $\theta=0$ . However, the concentration current  $\langle j_{C,x} \rangle_x$  does not vanish in general at the plates because of the different boundary conditions [Eq. (3)] for  $c$ .

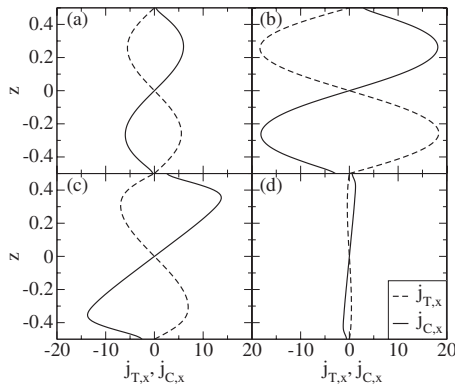


FIG. 5. Vertical profiles of averaged lateral currents sustained by TWs. Full and dashed lines show the currents of concentration,  $\langle j_{C,x} \rangle_x$ , and of heat,  $\langle j_{T,x} \rangle_x$ , respectively. The subfigures (a)–(d) correspond to the TW states that are identified by the points a–d in Fig. 3. Parameters are  $L=0.01$ ,  $\psi=-0.4$ , and  $\phi^*=1$ .

Following the TW branch from its bifurcation out of the conductive state up to  $R^*$ , the amplitudes of  $\langle j_{T,x} \rangle_x$  and of  $\langle j_{C,x} \rangle_x$  grow at first with growing amplitude of  $\Phi$ ,  $\theta$ , and  $\zeta$  modes. But then—say, beyond point c in Fig. 3—the amplitudes of the lateral averaged currents decrease again and the currents vanish as the TW branch ends at  $R^*$  in the SOC branch.

IV. INFLUENCE OF PARAMETERS

In this section, we discuss the consequences of changing the Lewis number  $L$ , the separation ratio  $\psi$ , or the normalized porosity  $\phi^*$  on the bifurcation behavior, the frequency, and the mixing behavior of TW states. The wave number  $k$  of all discussed TW structures remains fixed to  $\pi$ .

As noted already is the behavior of  $Nu-1$  and  $w_{11}^2$  similar. However, the Nusselt number of a binary mixture usually grows larger than the Nusselt number of a pure fluid whereas the leading amplitude  $w_{11}$  of the vertical velocity in a binary

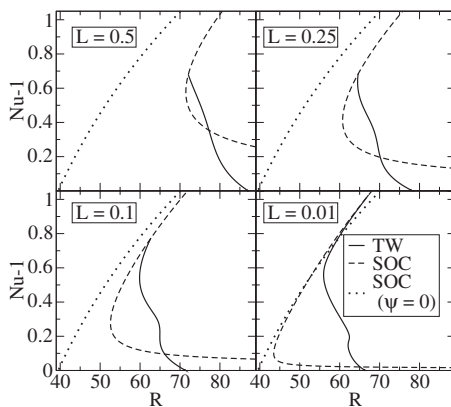


FIG. 6. Influence of the Lewis number  $L$  on the bifurcation behavior of TW and SOC solutions. Shown are diagrams of Nusselt number versus Rayleigh-Darcy number for different values of  $L$  with  $\psi=-0.4$  and  $\phi^*=1$  held fixed. For comparison, we plotted also the Nusselt number of a pure fluid (dotted).

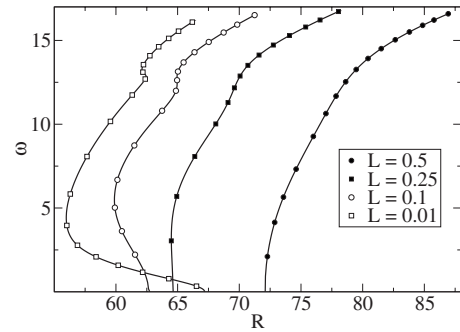


FIG. 7. Frequency  $\omega$  of TW convection versus Rayleigh-Darcy number  $R$  for different values of the Lewis number  $L$  with  $\psi=-0.4$  and  $\phi^*=1$  held fixed.

mixture with  $\psi < 0$  never exceeds the corresponding quantity in a pure fluid. We discuss in this section only Nu.

A. Variation of L

The influence of changing the Lewis number  $L$  on the bifurcation behavior is shown in Fig. 6. There, we plot the Nusselt number Nu of a SOC structure (dashed) and of a TW structure (solid) versus the Rayleigh-Darcy number  $R$  for different Lewis numbers. The dotted line denotes the Nusselt number of a pure fluid. Figure 7 shows the frequency of the TW structures along the TW branches that are shown in Fig. 6. The separation ratio and the normalized porosity is fixed throughout this subsection at  $\psi=-0.4$  and  $\phi^*=1$ , respectively.

The SOC branches in Fig. 6 look similar for all Lewis numbers. Their saddle points are shifted toward larger Rayleigh-Darcy numbers and larger Nu with increasing  $L$ . The influence of changing  $L$  on the TW structure is stronger. The Rayleigh-Darcy number  $R_{osc}$  of the bifurcation threshold grows with increasing  $L$ . The  $R$ -range of fast TW structures shrinks as  $L$  grows. When  $L$  becomes large enough, there are no forward oriented fast TW solutions anymore as can be seen in Fig. 6 for  $L=0.25$  and  $L=0.5$ . Moreover, the bifur-

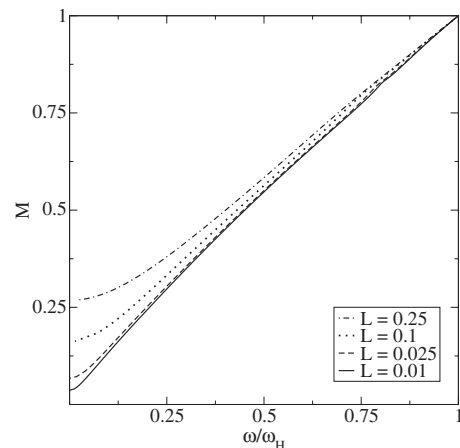


FIG. 8. Mixing number  $M$  of TW convection versus TW frequency  $\omega$  normalized by the Hopf frequency  $\omega_H$  for different Lewis numbers  $L$  with  $\psi=-0.4$  and  $\phi^*=1$  held fixed.

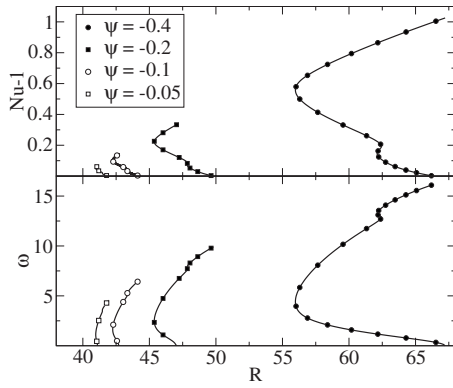


FIG. 9. Influence of the separation ratio  $\psi$  on the bifurcation behavior of TW convection. Shown are diagrams of the Nusselt number (top) and of the frequency (bottom) versus Rayleigh-Darcy number for different values of the separation ratio  $\psi$  with  $L=0.01$  and  $\phi^*=1$  held fixed.

cation point  $R^*$  approaches the SOC saddle point such that the region of forward curved slow TW solutions shrinks too. Finally, for  $L=0.5$ , the TW branch merges backward into the SOC branch and a forward oriented branch does not exist anymore.

As mentioned in Sec. III A, the behavior of the frequency  $\omega$  and of the mixing number  $M$  is qualitatively the same as in the system without porous medium [2,46]. For this system, numerical [46,48,49] as well as analytical investigations [48] have shown that  $M$  is approximately a linear function of  $\omega$ . Therefore, we plotted  $M$  versus the TW frequency  $\omega$  scaled by the Hopf frequency  $\omega_H$  of the oscillatory bifurcation threshold for different Lewis numbers in Fig. 8. For large frequencies, the curves differ only slightly and can be approximated by linear functions. For small frequencies, this does not hold anymore as a consequence of the boundary layers that arise (see Sec. III B). As in the ordinary Rayleigh-Bénard system [50], these layers prevent the value of the mixing number to fall below a certain value which grows with increasing Lewis number.

**B. Variation of  $\psi$**

Figure 9 shows the Nusselt number and corresponding TW frequencies for Lewis number  $L=0.01$ , normalized porosity  $\phi^*=1$  and different separation ratios  $\psi$ . The SOC so-

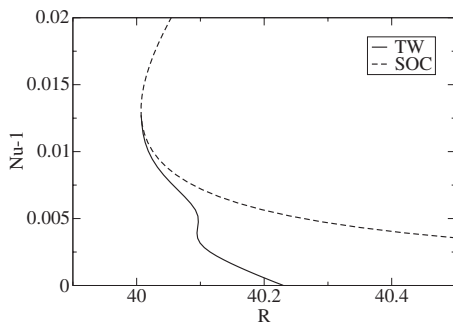


FIG. 10. Nusselt number versus Rayleigh-Darcy number of TW and SOC solutions for  $L=0.01$ ,  $\psi=-0.01$ , and  $\phi^*=1$ .

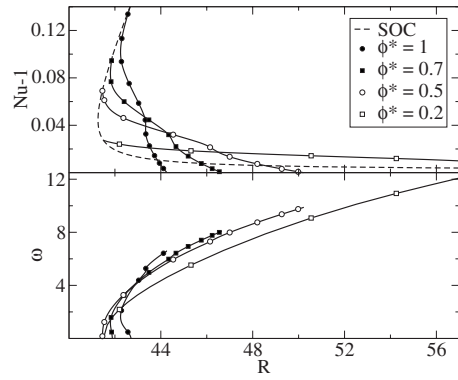


FIG. 11. Influence of the porosity on TW convection. Shown are diagrams of the Nusselt number (top) and of the TW frequency (bottom) versus Rayleigh-Darcy number for different values of the normalized porosity  $\phi^*$  with  $L=0.01$  and  $\psi=-0.1$  held fixed. For comparison, we also plotted the Nusselt number of the corresponding SOC structure (dashed).

lution branches look similar to the one for  $\psi=-0.4$ , thus they are not depicted.

The TW bifurcation branch as a whole is shifted toward smaller  $R$  as  $\psi$  approaches zero. In this process, the  $R$  range of the forward oriented branches of slow and fast TWs shrinks. However, there is still a small region in which a forward branch of fast TW solutions exists even for  $\psi=-0.05$ . When  $|\psi|$  is reduced further, another qualitative change in the bifurcation behavior happens as can be seen in Fig. 10. The TW branch (solid) merges backward with the lower SOC branch (dashed) such that a forward branch of slow TW structures does not exist anymore. However, a forward branch of fast TW structures still exists in an  $R$ -interval of about 0.002.

We found the mixing number  $M$  as a function of the reduced frequency  $\omega/\omega_H$  to be almost linear for all values of  $\psi$  as already depicted in Fig. 8 for varying  $L$ .

**C. Variation of  $\phi^*$**

The influence of the normalized porosity on the TW state is the most interesting one since there is no such parameter in the Rayleigh-Bénard system without porous medium. Figure 11 shows the bifurcation behavior of TW solutions for Lewis number  $L=0.01$ , separation ratio  $\psi=-0.1$ , and several normalized porosities  $\phi^*$ . The SOC solution branch shown by a dashed line is independent of  $\phi^*$ . The corresponding frequencies  $\omega$  are also shown in Fig. 11.

As already seen in Fig. 1, the bifurcation threshold  $R_{osc}$  as well as the Hopf frequency  $\omega_H$  increases with decreasing  $\phi^*$ . Moreover, the end point  $R^*$  of the TW solution branch moves with decreasing  $\phi^*$  downward along the SOC branch to smaller values of  $Nu$  thereby crossing the SOC saddle. For  $\phi^* < 0.2$ , no forward oriented part what so ever of the TW solution branch can be found anymore. The extension of the forward oriented branch of fast TWs close to  $Nu-1 \approx 0.04$  is already small for  $\phi^*=1$  and vanishes for  $\phi^* \leq 0.7$ .

As long as the normalized porosity is not too small, the mixing number  $M$  is again approximately a linear function of

the reduced frequency  $\omega/\omega_H$ . However, for small values of  $\phi^*$  deviations from this linear relation appear. Furthermore, the curve of mixing number versus reduced frequency is shifted upward.

## V. CONCLUSION

In this paper we investigated numerically the Rayleigh-Bénard system with porous medium saturated by a binary fluid mixture with negative separation ratio. We considered convection structures consisting of straight parallel rolls that are either stationary (SOC) or are traveling laterally (TW).

For an exemplary parameter set ( $L=0.01$ ,  $\psi=-0.4$ ,  $\phi^*=1$ ,  $k=\pi$ ), we discussed a typical bifurcation scenario in terms of the Nusselt number versus Rayleigh-Darcy number. Therein, the SOC solution branch is not connected to the quiescent, conductive ground state—it goes backward at small values of Nu until passing a saddle point and then it proceeds forward for larger Nu. The TW branch bifurcates backward out of the ground state and shows three saddle points. Here we can distinguish between slow and fast stable TWs as in the common Rayleigh-Bénard system without porous medium.

We investigated the behavior of velocity, temperature, and concentration fields along the TW branch. The temperature field is harmonic for all investigated values of  $R$ . On the other hand, the concentration field changes significantly with the advective flow amplitudes because of the strong connection between the concentration field and the streamlines in a reference frame that is comoving with the TW. The fact that the concentration field is largely determined by advection and almost behaves like a passive scalar is due to the smallness of the Lewis number, i.e., the smallness of concentration diffusion. To understand and to discuss the behavior of the streamlines that were determined with a full fledged nonlinear numerical analysis we used a single-mode stream func-

tion. In this way we found that closed streamlines arise when the velocity amplitude becomes larger than the phase velocity. The occurrence of closed streamlines in the  $x-z$  plane of the comoving frame marks a dramatic change in the shape of the concentration distribution—the profile of  $C$  develops for closed streamlines strong lateral anharmonicities.

We also investigated the vertical profiles of the laterally averaged horizontal currents of heat and concentration in a TW and found them to be nonzero. On the other hand, the TW does not support a mean lateral flow given that the linear Darcy law prevents Reynolds stresses. The currents vanish when all lateral modes of the fields are in phase, i.e., when the TW branch merges with the SOC branch. Due to its mirror symmetry in lateral direction, there can be no such currents in a SOC structure.

The qualitative features of the SOC branch do only change in the case of large Lewis numbers and separation ratios close to zero for which the SOC branch is connected to the ground state. The influence of parameter changes on the TW branch is stronger. When  $|\psi|$  decreases, the TW bifurcation branch as a whole is shifted toward smaller values of  $R$  without qualitative changes as long as the Lewis number  $L$  is small and the normalized porosity is large. With increasing  $L$ , the bifurcation threshold  $R_{\text{osc}}$  increases, the merging point  $R^*$  of the TW branch with the SOC solution branch approaches the SOC saddle point, and the  $R$  range of forward proceeding TWs decreases until there are no more saddle points along the TW branch. A similar behavior can be observed when decreasing the normalized porosity  $\phi^*$ . In addition, when  $\phi^*$  is decreased, the Hopf frequency of the TW structure grows. As in the Rayleigh-Bénard system without porous medium, the mixing number  $M$  is approximately a linear function of the frequency  $\omega$ . Differences from this linear relation for large  $L$  and small  $\omega$  can be explained to be due to boundary layers [50].

- 
- [1] M. C. Cross and P. C. Hohenberg, *Rev. Mod. Phys.* **65**, 851 (1993).
- [2] M. Lücke, W. Barten, P. Büchel, C. Fütterer, St. Hollinger, and Ch. Jung, *Lecture Notes in Physics Monographs* **55**, 127 (1998).
- [3] E. Bodenschatz, W. Pesch, and G. Ahlers, *Annu. Rev. Fluid Mech.* **32**, 709 (2000).
- [4] C. W. Horton and F. T. Rogers, *J. Appl. Phys.* **16**, 367 (1945).
- [5] E. R. Lapwood, *Proc. Cambridge Philos. Soc.* **44**, 508 (1948).
- [6] J. M. Straus, *J. Fluid Mech.* **64**, 51 (1974).
- [7] M. De La Torre Juárez and F. H. Busse, *J. Fluid Mech.* **292**, 305 (1995).
- [8] M. D. Shattuck, R. P. Behringer, G. A. Johnson, and J. G. Georgiadis, *J. Fluid Mech.* **332**, 215 (1997).
- [9] L. E. Howle, R. P. Behringer, and J. G. Georgiadis, *J. Fluid Mech.* **332**, 247 (1997).
- [10] M.-C. Charrier-Mojtabi, B. Elhajjar, and A. Mojtabi, *Phys. Fluids* **19**, 124104 (2007).
- [11] B. Elhajjar, M.-C. Charrier-Mojtabi, and A. Mojtabi, *Phys. Rev. E* **77**, 026310 (2008).
- [12] O. Sovran, M.-C. Charrier-Mojtabi, and A. Mojtabi, *C. R. Acad. Sci., Ser. Iib Mec.* **329**, 287 (2001).
- [13] O. Thomas, Ph.D. thesis, Stanford University, 2007.
- [14] K. Pruess, *Geothermics* **19**, 3 (1990).
- [15] M. J. O'Sullivan, K. Pruess, and M. J. Lippmann, *Geothermics* **30**, 395 (2001).
- [16] M. Ilyasov, I. Ostermann, and A. Punzi, *Handbook of Geomathematics* (Springer, Berlin, 2010), p. 679.
- [17] S. Saravanan and P. Kandaswamy, *Heat Mass Transfer* **39**, 693 (2003).
- [18] R. Umla, M. Augustin, B. Huke, and M. Lücke, *J. Fluid Mech.* **649**, 165 (2010).
- [19] C. Fütterer and M. Lücke, *Phys. Rev. E* **65**, 036315 (2002).
- [20] H. Tounsi, J. K. Platten, and G. Chavepeyer, *Eur. J. Mech. B/Fluids* **15**, 241 (1996).
- [21] R. Heinrichs, G. Ahlers, and D. S. Cannell, *Phys. Rev. A* **35**, 2761 (1987).
- [22] K. Lerman, D. S. Cannell, and G. Ahlers, *Phys. Rev. E* **59**,

- 2975 (1999).
- [23] B. L. Winkler and P. Kolodner, *J. Fluid Mech.* **240**, 31 (1992).
- [24] P. Kolodner, *Phys. Rev. E* **50**, 2731 (1994).
- [25] E. Moses, J. Fineberg, and V. Steinberg, *Phys. Rev. A* **35**, 2757 (1987).
- [26] E. Kaplan, E. Kuznetsov, and V. Steinberg, *Phys. Rev. E* **50**, 3712 (1994).
- [27] C. M. Surko, D. R. Ohlsen, S. Y. Yamamoto, and P. Kolodner, *Phys. Rev. A* **43**, 7101 (1991).
- [28] C. M. Aegerter and C. M. Surko, *Phys. Rev. E* **63**, 046301 (2001).
- [29] L. Ning, Y. Harada, and H. Yahata, *Prog. Theor. Phys.* **98**, 551 (1997).
- [30] O. Batiste, E. Knobloch, I. Mercader, and M. Net, *Phys. Rev. E* **65**, 016303 (2001).
- [31] D. Jung and M. Lücke, *Phys. Rev. Lett.* **89**, 054502 (2002).
- [32] D. Jung and M. Lücke, *Phys. Rev. E* **72**, 026307 (2005).
- [33] P. Matura, D. Jung, and M. Lücke, *Phys. Rev. Lett.* **92**, 254501 (2004).
- [34] D. Jung and M. Lücke, *EPL* **80**, 14002 (2007).
- [35] A. Alonso, O. Batiste, A. Meseguer, and I. Mercader, *Phys. Rev. E* **75**, 026310 (2007).
- [36] H. Brand and V. Steinberg, *Phys. Lett. A* **93**, 333 (1983).
- [37] E. Knobloch, *Phys. Rev. A* **34**, 1538 (1986).
- [38] In the definition of  $\gamma_a$  as given in Ref. [18], page 168, line 2, there is a typo. The correct formula reads  $\gamma_a = [K\lambda_{\text{tot}}\rho_0 / (d^2 C_{\text{tot}} \eta)] c_a$ .
- [39] D. A. Nield and A. Bejan, *Convection in Porous Media* (2006).
- [40] S. J. Linz, M. Lücke, H. W. Müller, and J. Niederländer, *Phys. Rev. A* **38**, 5727 (1988).
- [41] W. Barten, M. Lücke, W. Hort, and M. Kamps, *Phys. Rev. Lett.* **63**, 376 (1989).
- [42] W. Barten, M. Lücke, M. Kamps, and R. Schmitz, *Phys. Rev. E* **51**, 5636 (1995).
- [43] B. Huke, M. Lücke, P. Büchel, and Ch. Jung, *J. Fluid Mech.* **408**, 121 (2000).
- [44] St. Hollinger and M. Lücke, *Phys. Rev. E* **57**, 4238 (1998).
- [45] D. Jung, Ph.D. thesis, Universität des Saarlandes, 2005.
- [46] St. Hollinger, P. Büchel, and M. Lücke, *Phys. Rev. Lett.* **78**, 235 (1997).
- [47] M. Lücke, W. Barten, and M. Kamps, *Physica D* **61**, 183 (1992).
- [48] St. Hollinger, M. Lücke, and H. W. Müller, *Phys. Rev. E* **57**, 4250 (1998).
- [49] D. Jung, P. Matura, and M. Lücke, *Eur. Phys. J. E* **15**, 293 (2004).
- [50] St. Hollinger, Ph.D. thesis, Universität des Saarlandes, 1996.